Environ. Water Eng., 2025, 11(4), 473-485 https://doi.org/10.22034/ewe.2025.511425.2008

Environment and Water Engineering

Homepage: www.jewe.ir

ISSN: 2476-3683

Quantum-driven satellite imagery for enhancing evapotranspiration estimation in coastal areas

Zahra Rousta[1], Saeed Samadianfard[1]✉, Reza Delirhasannia[1], and Sadra Karimzadeh[2]

[1]Department of Water Engineering, Faculty of Agriculture, University of Tabriz, Iran

[2]Department of Remote Sensing and Geographic Information Systems, Faculty of Planning and Environmental Sciences, University of Tabriz, Tabriz, Iran

ARTICLE INFO

Paper Type: Research Paper

Received: 09 March 2025
Revised: 07 May 2025
Accepted: 10 May 2025
Published: 31 May 2025

Keywords
Evapotranspiration
Extreme Learning Machine
Hybrid Model
Satellite Image Data

Corresponding author:
S. Samadianfard
✉ s.samadian@tabrizu.ac.ir

ABSTRACT

Accurate assessment of water requirements for crops and large-scale, real-time water usage measurement is essential in water and soil management. Utilizing remote sensing data, which provides extensive spatial and temporal coverage, has emerged as a viable approach for evaluating evapotranspiration. The FAO-Penman-Monteith method is widely regarded as the most precise technique for computing reference evapotranspiration (ET_0). Extreme learning machines (ELM) models were employed alongside quantum computing optimization strategies (QIS-ELM), Bayesian optimization (BO-ELM), and particle swarm optimization (PSO-ELM). These models excel in processing complex datasets and recognizing patterns, thereby enhancing estimation accuracy. Daily meteorological data comprising temperature, relative humidity, wind speed, and sunlight hours, along with ET satellite imagery data from MODIS, covering the Ramsar and Babolsar stations from 2001 to 2023, were used as inputs for the models. To transform this data into daily figures, the Kalman filter and cubic spline interpolation techniques were applied. The performance evaluation of the models at both stations revealed that the PSO-ELM-8 model for Ramsar and the QIS-ELM-8 model for Babolsar achieved the highest accuracy, with error values of RMSE 0.19 and 0.28 mm/day, respectively, using satellite image data. Thus, the QIS-ELM and PSO-ELM models improve ET_0 estimation for coastal water management.

Highlights

- Hybrid models effectively predict ET using machine learning.
- Innovative satellite data integration improves ET estimation.
- Scenarios using MODIS data show varied model performance.

Citing:
Rousta, Z., Samadianfard, S., Delirhasannia, R., & Karimzadeh, S. (2025). Quantum-driven satellite imagery for enhancing evapotranspiration estimation in coastal areas. *Environment and Water Engineering*, *11*(4), 473-485. https://doi.org/10.22034/ewe.2025.511425.2008

1. Introduction

Evaporation is a physical process where water molecules gain energy to surpass the vapor pressure, transitioning from liquid to vapor more rapidly at elevated temperatures and lower air pressure (Malik et al., 2021). This phenomenon, occurring across bodies such as oceans, lakes, and rivers, contributes to atmospheric humidity. Evapotranspiration (ET) is a crucial hydrological cycle component, greatly influencing Earth's energy balance and necessitating afccurate estimation for water resource management (Teixeira et al., 2009; Li et al., 2003). ET involves water vapor loss from soil and plants and is essential for irrigation and water management (Mirhashemi and Panahi 2015; Feng et al., 2022). Proper ET assessment is crucial for sustainable water resource strategies, including irrigation planning and hydrological modeling (Kisi and Heddam 2019; Malik et al., 2020). Various ET estimation methods exist, ranging from field techniques to numerical modeling. These often start by estimating reference crop ET (ET_0), crucial for determining target crop-specific ET. Despite empirical methods' local calibration limitations, the FAO's Penman-Monteith method is the standardized approach for calculating ET_0, praised for its accuracy involving temperature, wind speed, and other crucial parameters (Allen et al., 2002; Allen et al., 1998). Although field and empirical methods can be impractical due to data access and spatial constraints, machine learning models now provide efficient

ET_0 estimation by integrating satellite imagery and empirical formulas, enhancing prediction quality (Gisolo et al., 2022).

Khari et al. (2023) compared artificial neural network models with empirical models namely Blaney-Criddle, Hargreaves-Samani, and Irmak for estimating ET_0 at the Ramhormoz synoptic station. They concluded that artificial neural network models exhibited superior correlation compared to empirical models, with the hybrid neural network model incorporating genetic algorithms achieving the highest alignment with the FAO-Penman-Monteith method. Similarly Amirzehni et al. (2023) evaluated spline and cubic spline methods for ET_0 estimation (2001–2021), using random forest (RF) and genetic algorithm-optimized random forest (GA-RF) models. Results demonstrated that cubic spline interpolation yielded greater accuracy than standalone spline methods. Additionally, integrating cubic spline interpolation with GA-RF models improved daily ET_0 estimation accuracy. Also, Samdianfard et al. (2024) applied Gaussian process regression (GPR), support vector regression (SVR), tree models (M5P), and linear regression models (M5Rules) to predict ET_0 using meteorological data from 1990 to 2021 at the Astara and Isfahan stations. Results indicated that the M5P model was the most effective for daily ET_0 forecasting at both locations.

Galehban et al. (2022) explored the feasibility of using WaPOR and ERA5 system products to compute daily ET_0 via the FAO-Penman-Monteith method and validated the results in Sistan and Baluchestan, Iran. Their findings showed a high degree of accuracy in satellite-derived products for daily ET_0 calculations. Similarly Talebi et al. (2022) highlighted the importance of satellite-derived parameters in improving ET_0 estimates at Tabriz and Babolsar stations. Gradient boosting and MLP models, using data from 2003 to 2021, incorporated variables such as day/night land surface temperatures, normalized difference vegetation index, and leaf area index. Results identified day and night land surface temperatures as the most influential factors for ET_0 estimation. To achieve effective water resource management, particularly for irrigation planning, accurate daily ET_0 estimation is crucial. Pandi et al. (2023) estimated evapotranspiration and crop coefficients of modified Hashemi rice during various growth phases using the SWAP model and satellite imagery at Rasht during the 2017-2018 growing season. The integration of satellite data with the SWAP model improved ET and crop coefficient estimates, underscoring the utility of satellite imagery in enhancing modeling efficiency. Also, Talebi et al. (2023) utilized stochastic gradient descent (SGD), multilayer perceptron (MLP), and a combined model (SGD-MLP) for daily ET_0 estimation in Tabriz (2003–2021), incorporating remote sensing and meteorological data. The SGD-MLP-11 configuration achieved the lowest error rate, with a coefficient of determination of 0.992. This study pioneers the integration of quantum computing with satellite imagery and extreme learning models for estimating ET_0 in coastal stations, a novel approach that has not been previously reported. By utilizing data from Ramsar and Babolsar stations (2001–2023), the research investigates the unique impact of coupling quantum computing frameworks with state-of-the-art machine learning techniques on ET_0 estimation accuracy. Also, the study examines the role of innovative data processing methods, such as Kalman filtering and cubic spline interpolation, in refining model outputs. The novelty lies in identifying the optimal combination of satellite-derived and meteorological variables to either enhance model accuracy or streamline data input requirements, assessed through rigorous performance and error evaluation metrics. Such a combination has not been previously studied in Babolsar and Ramsar using the QIS-ELM, BO-ELM, and PSO-ELM models. This research applies this approach for the first time in these regions, demonstrating that quantum optimization and machine learning methods can provide more precise and stable estimations for water and soil resource management.

2. Materials and Methods

2.1 Study area

In this research, the daily ET_0 was estimated utilizing meteorological data from two synoptic stations, Ramsar and Babolsar, situated in Mazandaran province, over a span of 23 years from 2001 to 2023. Ramsar is positioned at a latitude of 36° 52′ north and a longitude of 50° 40′ east, encompassing an area of 729.8 Km^2. Conversely, Babolsar, which covers an area of 13.5 Km^2, is located at a latitude of 36° 43′ north and a longitude of 52° 39′ east. The locations of the study stations created using ArcGIS software are illustrated in Fig. 1.

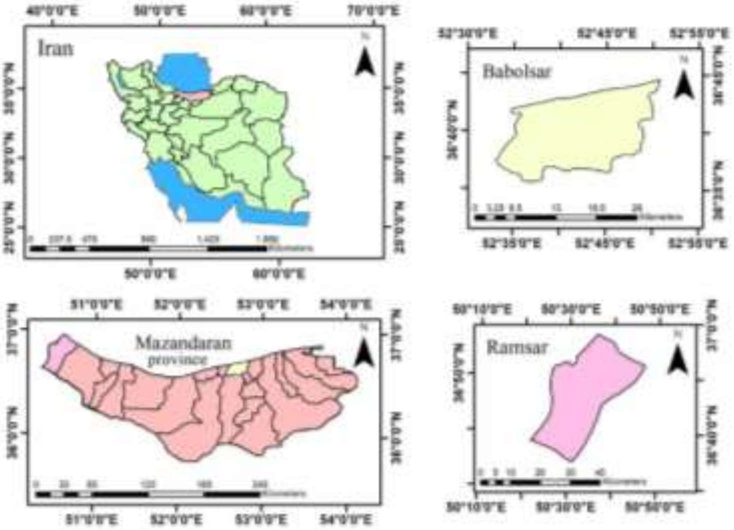

Fig. 1 Geographical map showing Ramsar and Babolsar stations, with relevant topographical features

2.2 Data and modeling methodology

The estimation of ET for the Ramsar and Babolsar stations was carried out using the ELM, QIS-ELM, BO-ELM, and PSO-ELM models, all of which were implemented in a Python programming environment. The dataset was divided into 70% for training and 30% for testing. The model inputs included both satellite imagery data and various meteorological factors. The meteorological variables considered were: minimum temperature (T_{min}), maximum temperature (T_{max}), average temperature (T_m), minimum relative humidity (U_{min}), maximum relative humidity (U_{max}), average relative humidity (U_m), average wind speed (ffm), and sunshine duration (SSHN). Additionally, satellite imagery data included MODIS-derived evapotranspiration. The Google Earth Engine platform facilitated the acquisition of satellite imagery within the Python environment, with the data systematically recorded at 8-day intervals.

In this research, the standard FAO-Penman-Monteith method was used to calculate ET as the reference method (Equation 1) (Allen et al., 2002; Allen et al., 1998).

$$ET_0 = \frac{0.408\Delta(R_n - G) + \gamma\frac{900}{T_m + 273}U_2(e_s - e_a)}{\Delta + \gamma(1 + 0.34U_2)} \qquad (1)$$

where Δ is the slope of the saturated water pressure-temperature curve (kPa.◦C^{-1}), R_n: net radiation (MJ.m^{-2}.d^{-1}), G: soil heat flux density (MJ.m^{-2}.d^{-1}), γ: represents the psychrometric constant (kPa.◦C^{-1}), e_s: saturated water pressure (kPa), and e_a: actual water pressure (kPa), and T_m is mean temperature (°C).

2.3 Scenario design and structuring

The statistical characteristics of the dataset used in this research are presented in Table 1. Figures 2 illustrate the heat maps of the employed parameters, generated using the Pearson correlation coefficient. Based on these heat maps and the correlation analysis, four scenarios were developed using only meteorological parameters, and another four scenarios that integrated both meteorological variables and MODIS-derived evapotranspiration, for the estimation of daily ET_0 (as detailed in Table 2). Specifically, the first scenario reflects the least correlation with ET_0, while the fourth scenario shows the highest correlation. Scenarios five through eight follow the same structure, organized by the Pearson correlation coefficient and incorporating evapotranspiration estimates from MODIS remote sensing data, in the same order as the previous scenarios.

Table 1 Statistical parameters of the datasets used in the study, including mean, standard deviation, and range

	variable	Unit	X_{mean}	X_{min}	X_{max}	S_x	C_v	C_{sx}
Ramsar	ffm	m/s	1.874	0	9.75	1.015	0.542	1.562
	T_{max}	°C	20.427	0.6	37	7.483	0.366	0.018
	T_{min}	°C	14.209	3.6	28.2	7.141	0.503	-0.036
	T_m	°C	17.319	-1.5	31	7.177	0.414	0.007
	U_{max}	%	89.887	51	100	6.1	0	-0.75363
	U_{min}	%	69.24	6	100	12	0	-0.69357
	U_m	%	80.539	31.5	100	8.004	0.099	-0.459
	SSHN	h	4.656	0	13.2	4.043	0.868	0.291
	ET_{pm}	mm	4.432	0.373	16.312	2.353	0.531	0.677
	ET_{modis}	mm	7.281	0.817	17.607	4.542	0.624	0.489
Babolsar	ffm	m/s	1.608	0	7.25	0.961	0.598	0.997
	T_{max}	°C	21.971	0.4	38.5	7.605	0.346	-0.063
	T_{min}	°C	14.974	-3.6	29	7.2	0.481	-0.054
	T_m	°C	18.474	-1.1	32	7.263	0.393	-0.026
	U_{max}	%	91.772	60	100	4.162	0	-0.89978
	U_{min}	%	64.779	20	95	10.856	0	0
	U_m	%	79.233	47.75	96.875	6.769	0.085	-0.321
	SSHN	h	5.825	0	12.6	3.906	0.671	-0.175
	ET_{pm}	mm	5.386	0.654	17.106	2.593	0.482	0.454
	ET_{modis}	mm	4.474	0.444	15.027	2.835	0.634	1.605

C_{sx} represents the overall cumulative deviations from the data's mean, serving as a tool for trend identification. C_v, on the other hand, denotes the proportion of the standard deviation relative to the mean, providing insight into the extent of data variability. Furthermore, S_x refers to the standard deviation itself, illustrating how data points spread around the mean. X_{min} indicates the minimum value, while X_{max} denotes the maximum value present in the dataset. X_{mean} also signifies the mean, reflecting the data's central tendency. Collectively, these parameters enable analysts to gain a deeper understanding of the dataset's fundamental characteristics.

Fig. 2 Heatmap of the implemented parameters at: a) Ramsar, and b) Babolsar station

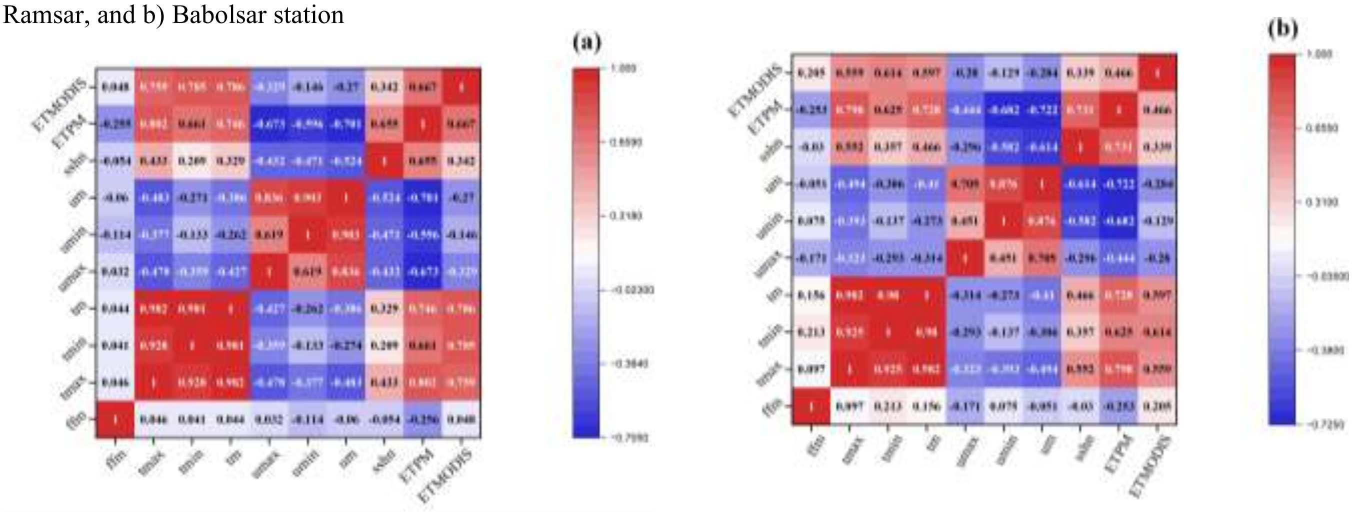

Table 2 Sequence of scenarios considered in the study

Number	Scenario
1	T_m, T_{min}, T_{max}
2	T_m, T_{min}, T_{max}, SSHN
3	T_m, T_{min}, T_{max}, SSHN, U_{max}, U_m, U_{min}
4	T_m, T_{min}, T_{max}, SSHN, U_{max}, U_m, U_{min}, ffm
5	T_m, T_{min}, T_{max}, ET_{modis}
6	T_m, T_{min}, T_{max}, SSHN, ET_{modis}
7	T_m, T_{min}, T_{max}, SSHN, U_{max}, U_m, U_{min}, ET_{modis}
8	T_m, T_{min}, T_{max}, SSHN, U_{max}, U_m, U_{min}, ffm, ET_{modis}

Generally, based on the correlation coefficients between the input data, illustrated in Fig. 2, we developed scenarios and presented the results in Table 2. At first, we formulated Scenarios 1 to 4 by ranking the correlation coefficients without incorporating MODIS evapotranspiration data. Then, we constructed Scenarios 5 to 8, this time factoring in the evapotranspiration derived from the MODIS sensor. Finally, the remaining necessary steps were carried out to complete the analysis. The presented flowchart in Fig. 3 provides a concise overview of all the steps involved in conducting this research. It visually represents the sequential process, highlighting key stages from initial planning to final analysis.

Fig. 3 Flowchart of the step-by-step procedure for estimating ET_0 in the study area

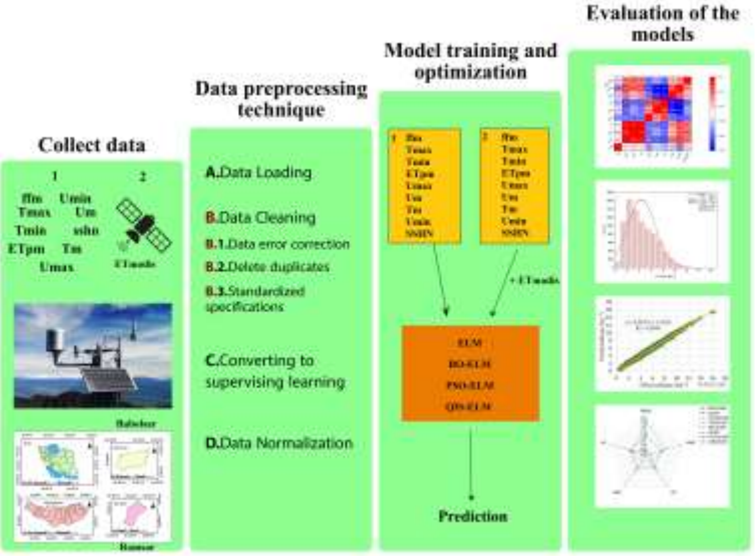

2.4 Extreme learning machine

Extreme Learning Machine (ELM) is an innovative machine learning technique designed for training neural networks. This algorithm has quickly become popular among researchers and experts due to its high learning speed and ease of implementation. The ELM model is recognized as a fast and effective method for training neural networks. By using random weights and a simple computational process, this model can perform well in various machine learning problems. Instead of training the input weights, this model assigns them randomly. This approach makes the learning process faster and easier. The ELM model also performs acceptably in various machine learning domains, including prediction and classification. The ELM model is described by Eq. 2.

$$H = f(W.X+\beta) \quad (2)$$

H represents the output of the network. *W* are the random input weights. *X* forms the input data. β is the network bias, and *f* is the activation function. After calculating *H*, the output weights β are calculated as Eq. 3:

$$\beta = H^{+}.T \quad (3)$$

where, H^{+} is the general inverse matrix of *H* and *T* represents the actual labels (Loizidis et al., 2025).

2.5 Bayesian Optimization Algorithm

Bayesian Optimization Algorithm (BO) is an efficient optimization method that is particularly designed for optimizing functions with high computational cost or functions that are time-consuming to evaluate. This method is applicable in the fields of machine learning. Bayesian optimization uses a probabilistic model to describe the objective function and thereby can manage the uncertainty in the evaluations. This method typically uses a surrogate function for the objective function, and can thereby select new points for evaluation.

2.6 Particle swarm optimization algorithm

Particle Swarm Optimization (PSO) is a population-based optimization algorithm that is designed to solve complex nonlinear optimization problems. This algorithm is inspired by the social behavior of living beings, such as birds or fish, who move in groups to find food or search for a path. It is widely used in many optimization problems due to its simplicity in implementation and high efficiency. In this algorithm, a population of particles or solutions moves simultaneously in the search space and searches for the best solution. Each particle uses its own best position and the best position of the group to determine a new position for itself. The main equations of PSO include the following steps (Bukhari et al., 2025):

- Updating the velocity of the particles (Eq. 4):

$$V_i^{t+1} = \omega . v_i^t + c_1 . r_1 . (p_i - x_i^t) + c_2 . r_2 . (g - \mathrm{x}_\mathrm{i}^\mathrm{t}) \quad (4)$$

Here, $\mathrm{v}_\mathrm{i}^\mathrm{t}$ is the velocity of particle *i* at time *t*. *ω* is the inertia weight. c_1 and c_2 are learning coefficients. r_1 and r_2 are random numbers between 0 and 1. $\mathrm{x}_\mathrm{i}^\mathrm{t}$ is the position of particle *i* at time *t*. p_i is the best position of particle *i* and g is the best group position.

- Update of particle positions (Eq. 5):

$$X_i^{t+1} = x_i^t + v_i^{t+1} \quad (5)$$

2.7 Quantum-Inspired Computing Algorithms

Quantum-Inspired Computing (QIS) refers to a set of methods and techniques that are inspired by quantum principles and concepts, but do not directly use quantum hardware. These algorithms are typically used in the fields of optimization, machine learning, and solving complex problems. These algorithms can effectively solve optimization problems and can outperform classical algorithms. Some of these algorithms are also used in machine learning and can help improve the accuracy and speed of models. Given the recent advancements in quantum science, these algorithms are rapidly evolving and improving. One of the most well-known of these algorithms is the Quantum Algorithm. Eqs. 6 to 8 show the key mathematical processes associated with this algorithm.

- Cost function (Eq. 6):

$$C(x) = \Sigma_i w_i f_i(x) \quad (6)$$

The cost function $C(x)$ must be minimized. w_i are the weights related to each function $f_i(x)$.

- Cost operator (Eq. 7)

$$U_c = e^{-i\gamma c} \quad (7)$$

that U_c is the cost operator, and γ is the optimization parameter.

- Final state (Eq. 8)

$$\psi_f = U_c^p U_B^p \psi_0 \quad (8)$$

That in which, ψ_f is the final state, U_B is the update operator, p is the number of iterations, and ψ_0 is the initial state (Ghosh et al., 2025).

2.8 Model evaluation criteria

In this study, various statistical metrics including the coefficient of determination (R^2) (Eq. 9), root mean square error (RMSE) (Eq. 10), Nash-Sutcliffe efficiency coefficient (NS) (Eq. 11), Willmott agreement index (WI) (Eq. 12), and Normalized Root Mean Square Error (NRMSE) (Eq. 13), were employed to assess the performance of the models through specific formulas (Amini et al., 2009). The WI index ranges from -1 to 1, while the NS coefficient can extend from negative infinity up to 1. A WI value of 1 denotes the highest level of precision, whereas a value of -1 signifies the lowest accuracy of the models. In terms of R^2 and RMSE, greater proximity to 1 and 0, respectively, indicates a stronger correlation and diminished error in the model (Amini, 2020).

$$R^2 = \left(\frac{\left(\Sigma_{i=1}^{N} OiPi - \frac{1}{N}\Sigma_{i=1}^{N} Oi\, \Sigma_{i=1}^{N} Pi\right)}{\left(\left(\Sigma_{i=1}^{N} Oi^2 - \frac{1}{N}\left(\Sigma_{i=1}^{N} Oi\right)^2\right)\left(\Sigma_{i=1}^{N} Pi^2 - \frac{1}{N}\left(\Sigma_{i=1}^{N} Pi\right)^2\right)\right)} \right)^2 \quad (9)$$

$$RMSE = \sqrt{\frac{1}{N}\Sigma_{i=1}^{N}(Pi - Oi)^2} \quad (10)$$

$$NS = 1 - \left[\frac{\Sigma_{i=1}^{N}(Oi - Pi)^2}{\Sigma_{i=1}^{N}\left(Oi - \overline{O}i\right)^2}\right] \quad (11)$$

$$WI = 1 - \left[\frac{\Sigma_{i=1}^{N}(Oi - Pi)^2}{\Sigma_{i=1}^{N}\left(|Pi - \overline{O}i| + |Oi - \overline{O}i|\right)^2}\right] \quad (12)$$

$$NRMSE = \frac{RMSE}{X_{max} - X_{min}} \quad (13)$$

In the above relations, *N* is the total number of data, $\overline{O}_i$ is the average of the observed values, and the parameters P_i and O_i are the predicted and observed values, respectively (Hashemi et al., 2025).

3. Results and Discussion

3.1 ET prediction results

To convert these observations into a daily format, two methods were employed: Kalman filtering and cubic spline interpolation. Kalman filtering is used to produce precise estimates of the system state over time, mitigating data variability, while cubic spline interpolation effectively links existing data points to produce daily data with improved accuracy. The integration of these techniques was essential for preparing satellite data for daily analysis.

To assess the influence of input parameters on the model outputs, eight distinct scenarios were explored, as outlined in Table 2. It should be noted that all computations and formula writing were performed using Python software, which facilitated efficient data processing and analysis. The discrepancies between observed and predicted values are presented in Tables 3 and 4, quantified using error metrics for both the Ramsar and Babolsar stations. At the Ramsar station, the ELM-1 model exhibited the least favorable performance, with an R^2 value of 0.64, RMSE of 1.37 (mm day^{-1}), NS of 0.64, and WI of 0.89, indicating a poor correlation between measured and predicted values. In contrast, the ELM-2 and ELM-3 models showed improved performance, with better R^2, NS, and WI values, alongside a slight reduction in RMSE. The ELM-4 model also demonstrated increased accuracy, similar to ELM-2 and ELM-3, likely due to the inclusion of additional parameters. When comparing ELM-5 to ELM-4, ELM-5 showed an R^2 of 0.72, RMSE of 1.21 (mm day^{-1}), NS of 0.72, and WI of 0.91, indicating a deterioration of 35% in R^2 and 67% in RMSE, likely due to fewer parameters used. Significant improvements were observed in the ELM-6 and ELM-7 models.

Table 3 Evaluation results for predictive models applied at Ramsar station, including accuracy and error rates

Method	R^2	RMSE	WI	NS	NRMSE
ELM 1	0.643	1.373	0.897	0.683	0.049
ELM 2	0.741	1.170	0.925	0.741	0.212
ELM 3	0.826	0.985	0.951	0.826	0.258
ELM 4	0.970	0.393	0.992	0.970	0.281
ELM 5	0.722	1.211	0.918	0.722	0.091
ELM 6	0.764	1.115	0.932	0.764	0.222
ELM 7	0.842	0.914	0.956	0.842	0.271
ELM 8	0.991	0.222	0.997	0.991	0.318
BO-ELM 1	0.744	1.162	0.922	0.744	0.048
BO-ELM 2	0.793	1.045	0.938	0.793	0.193
BO-ELM 3	0.856	0.871	0.959	0.856	0.236
BO-ELM 4	0.972	0.378	0.993	0.972	0.258
BO-ELM 5	0.764	1.115	0.929	0.764	0.088
BO-ELM 6	0.803	1.020	0.942	0.803	0.202
BO-ELM 7	0.868	0.833	0.963	0.868	0.242
BO-ELM 8	0.991	0.207	0.997	0.991	0.269
PSO-ELM 1	0.743	1.164	0.922	0.763	0.046
PSO-ELM 2	0.793	1.045	0.938	0.793	0.195
PSO-ELM 3	0.855	0.874	0.959	0.855	0.237
PSO-ELM 4	0.974	0.369	0.993	0.974	0.258
PSO-ELM 5	0.765	1.114	0.929	0.765	0.086
PSO-ELM 6	0.801	1.025	0.941	0.801	0.203
PSO-ELM 7	0.866	0.840	0.962	0.866	0.242
PSO-ELM 8	0.992	0.196	0.998	0.992	0.270
QIS-ELM 1	0.763	1.251	0.930	0.763	0.051
QIS-ELM 2	0.808	1.126	0.944	0.808	0.195
QIS-ELM 3	0.859	0.963	0.961	0.859	0.237
QIS-ELM 4	0.981	0.348	0.995	0.981	0.258
QIS-ELM 5	0.780	1.205	0.935	0.780	0.086
QIS-ELM 6	0.807	1.127	0.944	0.807	0.202
QIS-ELM 7	0.861	0.957	0.962	0.861	0.242
QIS-ELM 8	0.987	0.287	0.996	0.987	0.269

The ELM-8 model emerged as the best performer within the ELM framework, achieving an R^2 of 0.99, RMSE of 0.22 mm/da), NS of 0.99, and WI of 0.99, attributed to the incorporation of MODIS satellite ET data. Similarly, the BO-

ELM-1 model showed the largest errors among the BO-ELM variants, with an R^2 of 0.74, RMSE of 1.16 mm/day, NS of 0.74, and WI of 0.92. The performance of the first four BO-ELM scenarios was similar to the ELM models, with no significant difference in metrics. However, a substantial improvement in RMSE of approximately 83% was noted in BO-ELM-8 compared to BO-ELM-4, suggesting that MODIS ET data was key to this improvement. Thus, BO-ELM-8 was the best performer in the BO-ELM group, achieving superior accuracy. An evaluation of the QIS-ELM model revealed considerable variations between the first (QIS-ELM-1) and fifth (QIS-ELM-5) scenarios. The sixth scenario showed enhanced accuracy by including average sunshine hours, reducing RMSE by about 0.09 (mm day^{-1}) relative to QIS-ELM-5, while other metrics remained relatively stable. QIS-ELM-8 demonstrated optimal performance, with an R^2 of 0.99, RMSE of 0.21 (mm day^{-1}), NS of 0.99, and WI of 0.99, confirming its status as the most efficient within the QIS-ELM framework. The PSO-ELM model's performance also varied, with the first and fifth scenarios showing the weakest results, reflected in RMSE values of 1.164 and 1.114 (mm day^{-1}), respectively. PSO-ELM-3 showed improvements over the first and second scenarios. Notably, PSO-ELM-8, which included average wind speed as a parameter, achieved an impressive 58% reduction in error compared to the previous scenario. The sixth scenario showed a minor improvement over the fifth, with PSO-ELM-6 reducing error by 8%. Ultimately, PSO-ELM-8 emerged as the best performer within the PSO-ELM models, with an R^2 of 0.99, RMSE of 0.196 (mm day^{-1}), NS of 0.99, and WI of 0.99. The comparative analysis of the models for estimating daily ET_0 at the Ramsar station highlighted that PSO-ELM-8 exhibited the highest accuracy across all models, demonstrating the most reliable performance.

Table 4 Evaluation results for predictive models applied at Babolsar station, including accuracy and error rates

Method	R^2	RMSE	WI	NS	NRMSE
ELM 1	0.217	2.838	0.756	0.217	0.059
ELM 2	0.649	1.523	0.904	0.649	0.209
ELM 3	0.812	1.114	0.948	0.812	0.255
ELM 4	0.981	0.350	0.995	0.981	0.373
ELM 5	0.428	1.944	0.854	0.428	0.067
ELM 6	0.734	1.326	0.926	0.734	0.214
ELM 7	0.821	1.087	0.952	0.821	0.292
ELM 8	0.985	0.307	0.996	0.985	0.545
BO-ELM 1	0.761	1.257	0.929	0.761	0.056
BO-ELM 2	0.805	1.135	0.943	0.805	0.187
BO-ELM 3	0.853	0.985	0.959	0.853	0.214
BO-ELM 4	0.982	0.340	0.995	0.982	0.231
BO-ELM 5	0.780	1.204	0.935	0.780	0.065
BO-ELM 6	0.812	1.114	0.945	0.812	0.189
BO-ELM 7	0.855	0.976	0.960	0.855	0.218
BO-ELM 8	0.987	0.292	0.996	0.987	0.241
PSO-ELM 1	0.763	1.252	0.929	0.763	0.057
PSO-ELM 2	0.801	1.146	0.942	0.801	0.188
PSO-ELM 3	0.859	0.965	0.960	0.729	0.213
PSO-ELM 4	0.981	0.349	0.995	0.981	0.231
PSO-ELM 5	0.780	1.205	0.935	0.780	0.067
PSO-ELM 6	0.814	1.108	0.946	0.814	0.185
PSO-ELM 7	0.854	0.980	0.960	0.954	0.220
PSO-ELM 8	0.986	0.259	0.996	0.986	0.240
QIS-ELM 1	0.763	1.251	0.930	0.763	0.055
QIS-ELM 2	0.808	1.126	0.944	0.808	0.184
QIS-ELM 3	0.859	0.963	0.961	0.859	0.216
QIS-ELM 4	0.981	0.348	0.995	0.981	0.231
QIS-ELM 5	0.780	1.205	0.935	0.780	0.067
QIS-ELM 6	0.807	1.127	0.944	0.807	0.185
QIS-ELM 7	0.861	0.957	0.962	0.861	0.216
QIS-ELM 8	0.987	0.287	0.996	0.987	0.240

To compare the performance and effectiveness of remote sensing data, we analyzed Scenario 5, which includes fewer temperature data points but incorporates evapotranspiration data from remote sensing sources. Our findings indicate that even with fewer input data, ET can still be estimated, although the error margin slightly increases. To enhance accuracy, we utilized a larger dataset along with ET_0 data from the MODIS sensor. As shown in Tables 3 and 4, integrating remote sensing data in Scenario 5 compared to Scenario 1 has resulted in a lower error rate, demonstrating improved estimation precision. For example, in the ELM model at Ramsar station, Scenario 5 showed around 12% improvement compared to Scenario 1. This improvement is due to the addition of the evapotranspiration parameter from the MODIS sensor, which helped enhance the model's accuracy.

The results of the models utilized at the Babolsar station are summarized in Table 4. In the case of the ELM model, an analysis of scenarios 1 and 4 reveals a significant reduction in the R^2 criterion. A similar pattern is evident when comparing scenarios 5 and 8. This indicates that scenario 8 demonstrates a notable enhancement in performance relative to scenario 4, attributed to the incorporation of the MODIS satellite-derived ET product. Between scenarios 5 and 7, although there is a slight decline in index values, the error rate exhibits a reduction of approximately 75.5% in comparison to scenario 4. Consequently, scenario 8 stands out with superior performance against other scenarios owing to its increased number of input factors. For the BO-ELM model, scenario 1 displays the highest error metrics among its counterparts, with an R^2 of 0.76, RMSE of 1.25 (mm day^{-1}), NS of 0.76, and WI of 0.92. Scenario 2, however, reveals no significant changes in error values or other performance criteria. A statistical assessment of scenarios 3 and 4 indicates a reduction in error of about 65.4%, along with a 15.2% increase in the NS value. Furthermore, the comparison of scenarios 5 and 6 shows no substantial variation in error rates against scenario 2. A comparative analysis of scenarios 7 and 8 highlights a remarkable decrease of approximately 70% in RMSE, signifying improved model efficacy in the final scenario. Ultimately, the overall evaluation identifies BO-ELM-8 as the model with the highest accuracy, featuring an R^2 of 0.98, RMSE of 0.29 (mm day^{-1}), NS of 0.98, and WI of 0.99. An assessment of the various QIS-ELM model scenarios reveals a decrease of around 1.72% in RMSE, alongside slight enhancements in other metrics. This improvement in RMSE for QIS-ELM-8 can be attributed to the inclusion of the average wind speed variable. Evaluation indices for scenarios five and six remained largely consistent. Ultimately, QIS-ELM-8 exhibited superior performance with an R^2 of 0.98, RMSE of 0.28 (mm day^{-1}), NS of 0.98, and WI of 0.99, outperforming other evaluated scenarios.

Additionally, a comparison of the results from the first and second scenarios of the PSO-ELM model indicates that the second scenario achieved an 8.5% enhancement in the error index, with other metrics showing minimal change. Analysis of scenarios five and six indicates no performance improvement, similar to the observations between the first and second scenarios, where there was a slight enhancement in error performance. In the final scenario, the value of the error index decreased by approximately 15.2% compared to scenario four, while other criteria maintained relative stability. Consequently, PSO-ELM-8 was designated as the most precise model, demonstrating an R^2 of 0.98, RMSE of 0.29 (mm day^{-1}), NS of 0.98, and WI of 0.99. In summary, the overall assessment of the models utilized for estimating daily ET_0 at the Babolsar station indicates that QIS-ELM-8 exhibits the best performance among all models and is therefore regarded as the optimal choice. Furthermore, the QIS-ELM-4 model also demonstrated commendable performance. Therefore, in the absence of the MODIS evapotranspiration product, the QIS-ELM-4 model, relying solely on meteorological parameters, serves as a promising alternative option.

3.2 Visual illustrations of the accuracy of implemented methods

Fig. 4 presents radar diagrams illustrating climatic factors influencing ET_0 at the Ramsar and Babolsar stations, respectively.

Fig. 4 Radar diagram at: a) Ramsar, and b) Babolsar stations

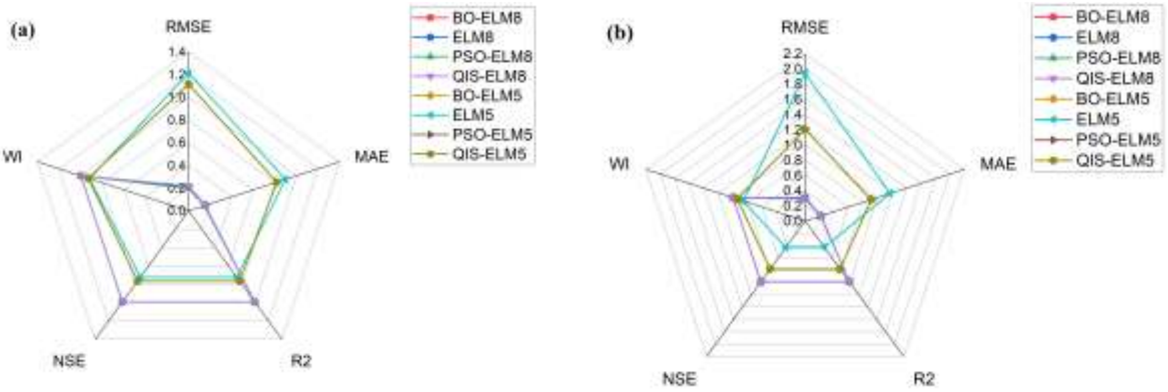

Additionally, Fig. 5 presents scatterplots for the Ramsar and Babolsar stations, respectively, providing a detailed visual representation of the relationship between key climatic variables and ET_0. Scatterplots are an effective tool for illustrating correlations, allowing readers to observe patterns and trends in the data points associated with each location.

Fig. 5 Scatter plot of observed versus predicted values, illustrating model fit: a) Ramsar, and b) Babolsar Stations

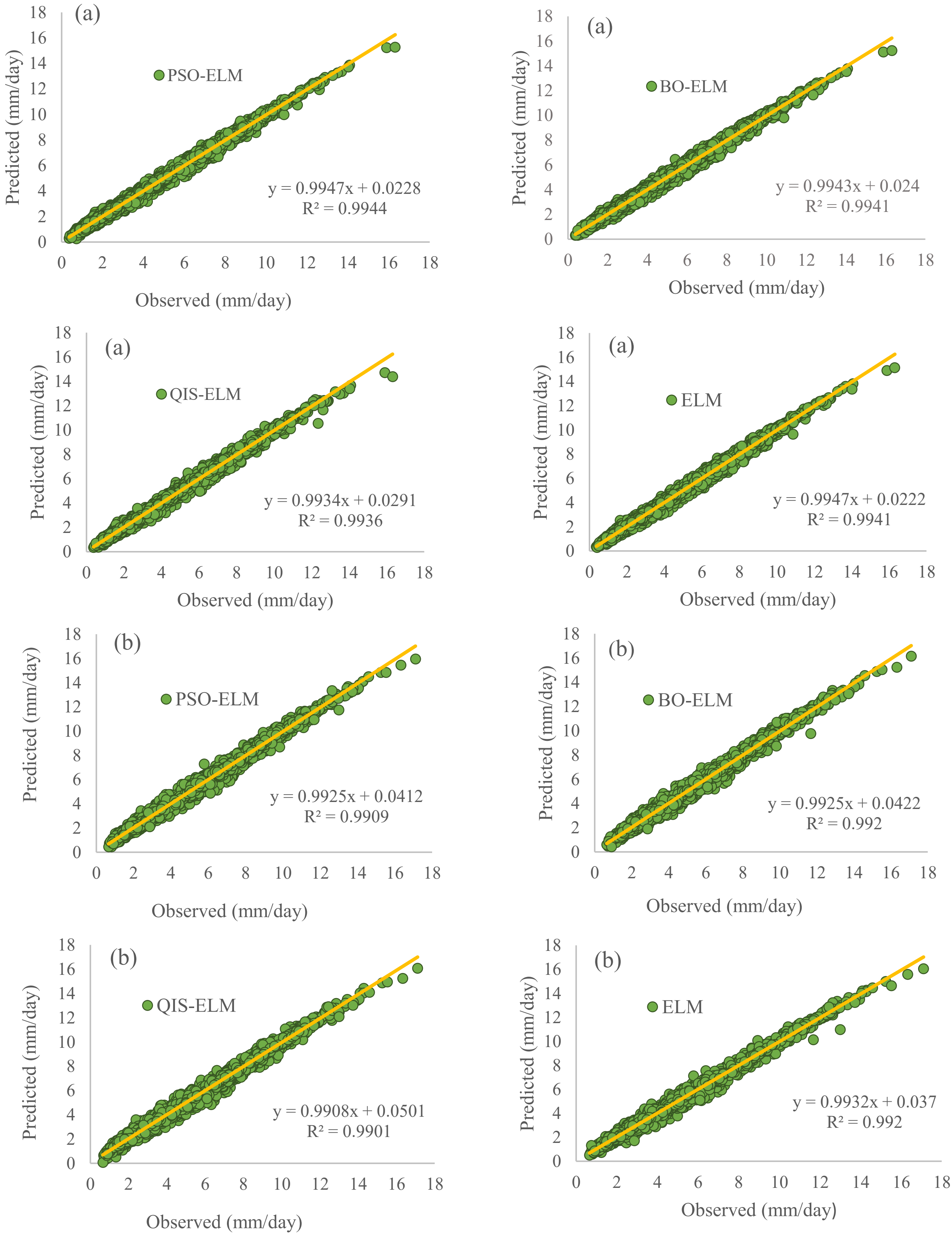

Fig. 6 displays violin plots for the Ramsar and Babolsar stations, respectively, summarizing the distribution and density of ET_0 values across varying climatic conditions. Violin plots effectively illustrate both the central tendency and variability of the data, providing a comprehensive overview of ET$_0$ dynamics. In Fig. 6.a, the Ramsar station's violin plot reveals distinct seasonal patterns in ET$_0$ distribution, indicating higher values during summer due to increased temperatures and solar radiation, with narrower sections seen in the winter months reflecting cooler conditions. Analyzing the median values and interquartile ranges enhances the understanding of typical evapotranspiration throughout the year, while outliers could signal extreme weather events worth investigating further. Conversely, Fig. 6.b presents the Babolsar station's violin plot, which may show a more uniform ET$_0$ distribution across seasons. A consistent pattern could occur due to higher humidity levels that moderate evaporation rates compared to Ramsar.

Fig. 6 Violin diagram: a) Ramsar, and b) Babolsar stations

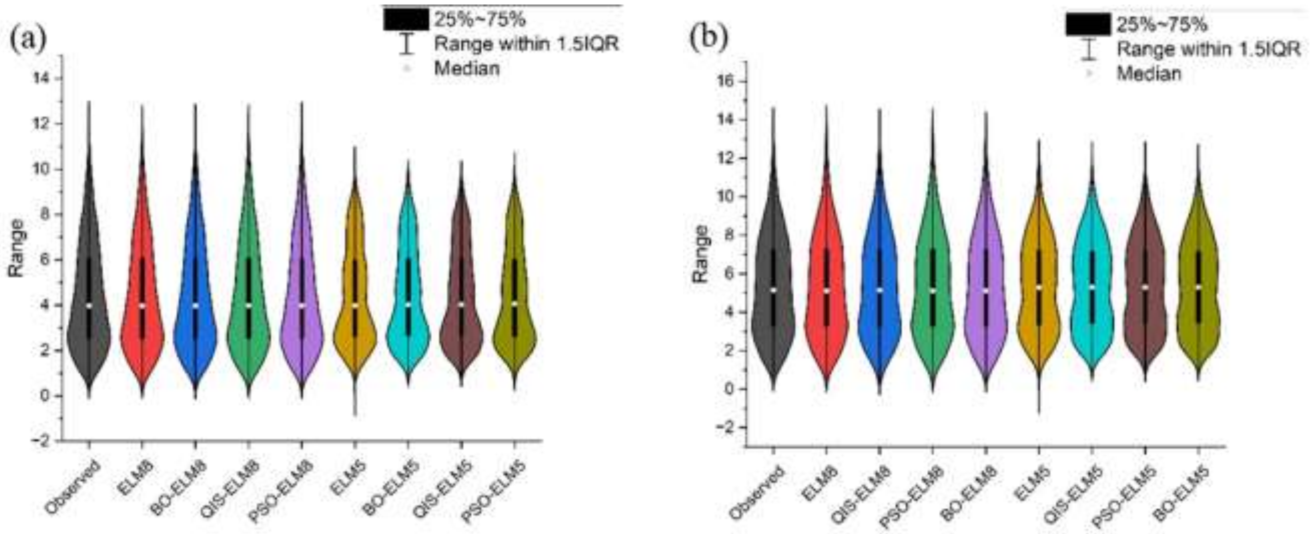

Fig. 7 presents the distribution charts for the Babolsar and Ramsar stations, offering a visual examination of the variations in ET$_0$. Distribution charts serve to depict how ET$_0$ values are spread across different ranges, demonstrating critical insights into the local ET$_0$ dynamics influenced by climatic factors. In Figs. 7e to 7h, the distribution chart for the Babolsar station reveals a relatively symmetrical distribution of ET$_0$ values, suggesting a stable range of ET$_0$ throughout the observation period. The peak of the distribution may indicate the most common ET$_0$ values experienced in Babolsar, reflecting the moderated climatic influences at this site, such as consistent humidity levels and equable temperature averages. The chart's spread indicates that while most ET$_0$ values cluster around a central point, there are occasional occurrences of higher ET$_0$ values, potentially attributable to seasonal variations or abrupt climatic shifts that encourage increased evaporation. Conversely, Figures 7a to 7d highlight the distribution of ET$_0$ at the Ramsar station. This chart may display a more pronounced right skew, indicating that a significant portion of ET$_0$ readings is clustered at lower values, with fewer instances of higher evapotranspiration.

3.3 Comparative analysis with existing literature

The findings of the present study indicate that all hybrid models, namely BO-ELM, PSO-ELM, and QIS-ELM, provide a more precise estimation of ET$_0$ compared to the ELM model, with no significant variations observed in the eighth scenario. Furthermore, the outcomes of this research align with those reported by Moshtagh et al. (2021), who estimated ET$_0$ by merging remote sensing data with the FAO-Penman-Monteith approach in the semi-arid agricultural landscapes of western Isfahan province. Their investigation revealed that the combination of remote sensing data and the FAO-Penman-Monteith method demonstrated exceptional efficacy in accurately estimating and mapping actual ET, making it a viable tool for developing water productivity maps for crops across various regions of the country. The results showed that agricultural lands had the highest evapotranspiration rate in the region, reaching 6.9 mm/day, while barren lands exhibited the lowest rate at 0.12 (mm day^{-1}). Therefore, this method can serve as a valuable complement to field-based techniques for determining plant water requirements. Chia et al. (2020) conclude that hybrid artificial intelligence models employing techniques such as data fusion, ensemble modeling, data decomposition, and remote sensing-based hybridization effectively overcome the limitations of individual models in evapotranspiration estimation. Integrating meteorological and satellite data significantly improves ET accuracy. A comprehensive literature review of studies published between 2011 and 2019 confirms the up-to-date and relevant framework of the research. Amirashayeri et al. (2023) predicted reference evapotranspiration (ET$_0$) by employing hybrid and intelligent methods. The authors combine machine learning models such as artificial neural networks (ANN) and tree-based techniques with an advanced pre-processing algorithm (ensemble empirical mode decomposition, EEMD) to reduce noise in the data. Applied to daily meteorological data from several stations in northwestern Iran, the results demonstrate that the hybrid approach significantly outperforms individual models by lowering prediction errors.

Fig. 7 Distribution diagram of observational data frequency and spread: a) ELM, b) QIS-ELM, c)PSO-ELM, d) BO-ELM, e) ELM, f) QIS-ELM, g) PSO-ELM, and h) BO-ELM

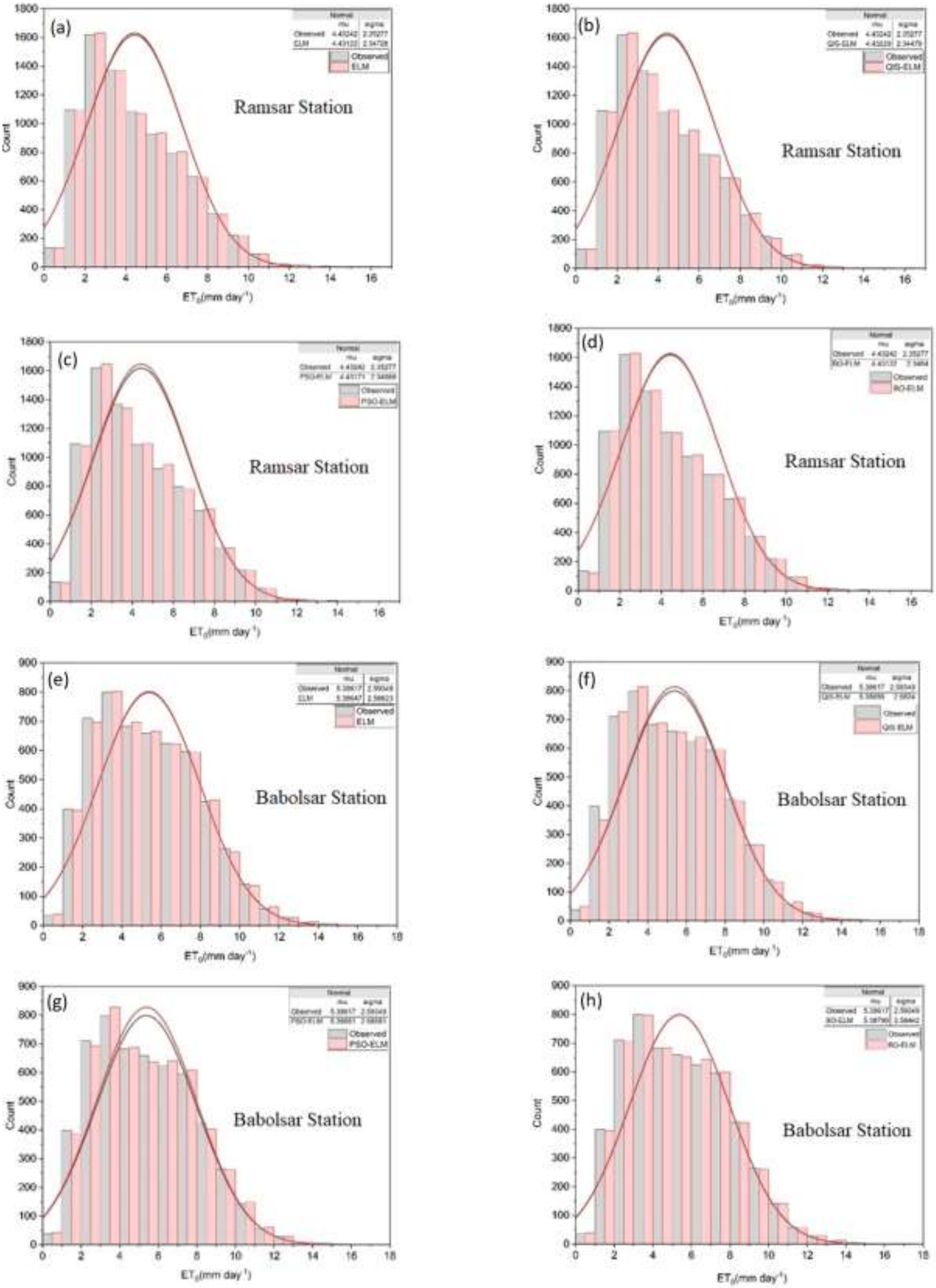

4. Conclusion

Evapotranspiration is influenced by key environmental factors such as solar radiation, temperature, humidity, wind speed, vegetation cover, and soil moisture. This study presents an in-depth analysis of ET_0 estimation, utilizing advanced machine learning techniques combined with satellite data over 23 years at the Ramsar and Babolsar stations. By incorporating meteorological variables, including temperature, relative humidity, wind speed, and sunshine hours, alongside MODIS satellite imagery, a comprehensive methodological framework was developed, leveraging the capabilities of Google Earth Engine. Based on the results of this study, the following conclusions can be drawn:

1. Model Integration Efficiency: Satellite data integration into machine learning models greatly enhances ET_0 estimation accuracy, with PSO-ELM-8 and QIS-ELM-8 proving most effective for Ramsar and Babolsar stations, respectively.

2. Importance of Input Selection: Careful input variable selection, particularly the inclusion of the satellite-derived evapotranspiration, is critical for improved predictive performance.

3. Satellite Imagery and Quantum Computing Importance: Use of MODIS satellite imagery enhances the accuracy of ET_0 estimations, while QIS-ELM leverages the power of quantum computing to enhance computational speed and predictive accuracy.

Limitations and Future Directions: The integration of advanced methods, such as quantum computing in conjunction with satellite data, presents challenges that warrant careful consideration in future research. Although quantum computing has the potential to enhance data processing capabilities, there are inherent complexities in its implementation. The current infrastructure relies primarily on classical computing, which can limit the efficiency of quantum algorithms. Furthermore, the compatibility of quantum computing frameworks with existing machine learning and data fusion techniques requires thorough investigation. Critical challenges include the need for specialized programming skills and the optimization of algorithms to ensure they leverage the unique properties of quantum processing.

Statements and Declarations

Data availability

The data can be sent by email from the Corresponding author upon request.

Conflicts of interest

The author of this paper declared no conflict of interest regarding the authorship or publication of this paper.

Author contribution

Z. Rousta: Data collection, data visualization, data analysis, and interpretation; S. Samadianfard: Research design, interpretation of results; R. Delirhasannia: Structural and content editing; S. Karimzadeh: Data analysis, drafting and revision.

AI Use Declaration

Portions of the language editing and writing refinement in this manuscript were assisted by the use of artificial intelligence tools, under the full supervision and final approval of the authors.

References

Allen, R. G. (1996). Assessing integrity of weather data for use in reference evapotranspiration estimation. *Journal of Irrigation and Drainage Engineering, 122*(2), 97-106, DOI:10.1061/(ASCE)0733-9437(1996)122:2(97).

Allen, R. G., Bastiaanssen, W. G. M., Wright, J. L., Morse, M., & Tasumi, R. T. (2002). Evapotranspiration from Satellite Image for Water Management and Hydrological Balances. Proceedings of the 2002 ICID Conference. Montreal. Canada. 1-12.

Allen, R.G., Pereira, L.S., Raes, D. & Smith, M. (1998). Crop Evapotranspiration (Guidelines for Computing Crop Water Requirements). FAO Irrigation and Drainage Paper 56. Food and Agricultural Organization of the United Nations. Rome. 17-18.

Amini, A. (2020). The role of climate parameters variation in the intensification of dust phenomenon. *Natural Hazards.* DOI: HTTPS://DOI.ORG/10.1007/S11069-020-03933-W.

Amini, A., Ali, T. M., Ghazali, A. H. B., Huat, B. K. (2009). Adjustment of Peak Streamflows of a Tropical River for Urbanization. *American Journal of Environmental Sciences*, *5*(3), 285-294, DOI: 10.3844/AJESSP.2009.285.294.

Amirashayeri, A., Behmanesh, J., Rezaverdinejad, V., Fathollahzadeh Attar, N. (2023). Evapotranspiration estimation using hybrid and intelligent methods. *Soft Computing, 27*, 9801-9821, DOI: HTTPS://DOI.ORG/10.1007/S00500-023-07822-9.

Amirzehni, P., Samadianfard, S., Nazemi, A.H., Sadraddini, A.A. (2023). Evaluating capabilities of the spline and cubic spline interpolation functions in reference evapotranspiration estimation implementing satellite image data. *Journal of Earth Science Informatics 16*(1), 3779-3795, DOI:10.1007/S12145-023-01127-Z [In Persian].

Bukhari, H., Basingab, M.S., Rizwan, A., Sánchez-Chero, M., Pavlatos, C., More, L.A.V., Fotis, G. (2025). Sustainable green supply chain and logistics management using adaptive fuzzy-based particle swarm optimization. *Sustainable Computing: Informatics and Systems. 46*, 101119.

Chia, M.Y., Huang, Y. F., HoonKoo, Ch., Fung, K. F. (2020). Recent Advances in Evapotranspiration Estimation Using Artificial Intelligence Approaches with a Focus on Hybridization Techniques-A Review. *Agronomy (MDPI), 10*(1), 101, DOI: HTTPS://DOI.ORG/10.3390/AGRONOMY10010101.

Galehban, E., Hamzeh, S., Veysi, SH., Alavipanah, S.K. (2022). Estimation of Daily Reference Evapotranspiration Using Remote Sensing Data (Case Study: Sistan and Baluchestan Province. *Iranian Journal of Remote Sensing* *and GIS, 14*(2), 37-50, DOI:10.52547/GISJ.14.2.37 [In Persian].

Ghosh, S., Kuila, P., Bey, M., Azharuddin, M.d. (2025). Quantum-inspired gravitational search algorithm-based low-price binary task offloading for multi-users in unmanned aerial vehicle-assisted edge computing systems. *Expert Systems with Applications, 263*, 125762.

Gisolo, D., Previati, M., Bevilacqua, I., Canone, D., Boetti, M., Dematteis, N., Balocco, J., Ferrari, S., Gentile, A., N'sassila, M. (2022). A calibration free radiation driven model for estimating actual evapotranspiration of mountain grasslands (CLIME-MG). *Journal of Hydrology, 610*(12), 127-138, DOI:10.1016/J.JHYDROL.2022.127948 [In Persian].

Hashemi, S., Samadianfard, S., Nazemi, A.H. (2025). Sequence-to-sequence and meta LSTM techniques enhanced by remote sensing for advanced evapotranspiration estimation. *Earth Science Informatics, 18*, 386. DOI: HTTPS://DOI.ORG/10.1007/S12145-025-01896-9.

Khari, D., Agdernazhad, A., Ebrahimipak, N. (2023). Comparison of artificiall intelligence models and experimental models in estimating reference evapotranspiration (case study: Ramhormoz synoptic station). *Water and Soil Management and Modeling, 3*(2), 112-124, DOI:10.22098/MMWS.2022.11293.1117.

Kisi, O., Heddam, S. (2019). Evaporation modelling by heuristic regression approaches using only temperature data. *Hydrological Sciences Journal, 64*(6), 653-672, DOI:10.1080/02626667.2019.1599487.

Li, Y.L., Cui, J.Y., Zhang, T.H., Zhao, H. Li. (2003). Measurement of evapotranspiration of irrigated spring wheat and maize in a semi-arid region of North China. *Agricultural Water Management, 61*(1),1-12, DOI:10.1016/S0378-3774(02)00177-4.

Loizidis, S., Venizelou, V., Kyprianou, A., Georghiou, G.E. (2025). Integrating PNN classification and ELM-Bootstrap for enhanced Day-Ahead negative price forecasting. *Applied Energy, 392*, 126013, DOI: HTTPS://DOI.ORG/10.1016/J.APENERGY.2025.126013 .

Malik, A., Kumar, A., Kim, S., Kashani, M.H., Karimi, V., Sharafati, A., Ghorbani, M.A., Al-Ansari, N., Salih, S.Q., Yaseen, Z.M. (2020). Modeling monthly pan evaporation process over the Indian central Himalayas: Application of multiple learning artificial intelligence model. *Engineering Applications of Computational Fluid Mechanics, 14*(1), 323-338, DOI:10.1080/19942060.2020.1715845.

Malik, A., Tikhamarine, Y., Al-Ansari, N., Shahid, S., Sekhon, H.S., Pal, R.K., Rai, P., Pandey, K., Singh, P., Elbeltagi, A., Sammen,, S.S. (2021). Daily pan-evaporation estimation in diferent agro-climatic zones using novel hybrid support vector regression optimized by Salp swarm algorithm in conjunction with gamma test. *Engineering Applications of Computational Fluid Mechanics, 15*(1), 1075- 1094, DOI:10.1080/19942060.2021.1942990.

Mirhashemi, S.H., Panahi, M. (2015). Evaluation of a data mining model in predicting of" average temperature" and potential evapotranspiration month for the next month in the synoptic weather station Yazd. *Biological Forum, 7*(1), 1469-1473, DOI: HTTP://DX.DOI.ORG/10.29252/JWMR.9.18.157.

Moshtagh, N., Jafari, R., Soltani, S., Ramezani, N. (2021). Integrating FAO-56 and Remotely-Sensed Techniques for Estimating Actual Evapotranspiration in Semi-arid Region of Isfahan Province. *Iranian Society of Range management, 4*(1), 638-648, DOI: HTTPS://DOR.ISC.AC/DOR/20.1001.1.20080891.1400.15.4.5.6.

Pandi, H., Asadi Kapourchal, S., Vazifedoust, M., Rezaei, M. (2023). Evaluation of the performance of SWAP model updated with satellight data in estimating of rice evapotranspiration and its crop coefficients. *Iranian Journal of Soil And Water Research, 54*(8), 1197-1213, DOI:10.22059/IJSWR.2023.361733.669525.

Samadianfard, S., Rousta, Z., Sharafi, M. (2024). Prediction of daily reference evapotranspiration with M5P, Gaussian process regression and Support vector regression methods. *Journal of Water and Soil, 34*(2), 156-176, DOI:10.22034/WS.2024.58879.2541.

Talebi, H., Samadianfard, S., Valizadeh Kamran, Kh. (2022). Investigating the roles of different extracted parameters from satellite images in improving the accuracy of daily reference evapotranspiration estimation. *Journal of Applied Water Science, 13*(2), 59-70, DOI:10.1007/S13201-022-01862-6.

Talebi, H., Samadianfard, S., Valizadeh Kamran, Kh. (2023). Estimation of daily reference evapotranspiration implementing satellite image data and strategy of ensemble optimization algorithm of stochastic gradient descent with multilayer perceptron. Environment. *Development and Sustainability, 27*(2), 3707-3729, DOI:10.1007/S10668-023-04037-8.

Teixeira, A.H., Bastiaanssen, W.G.M., Ahmad M.D., Bos M.G. (2009). Reviewing SEBAL input parameters for assessing evapotranspiration and water productivity for the Low-Middle Sao Francisco River basin, Brazil. Part A: Calibration and validation. *Agricultural and Forrest Meteorology, 149*(3-4), 462-476, DOI:10.1016/J.AGRFORMET.2008.09.014.